New insights into eruption source parameters of the 1600 CE Huaynaputina Plinian eruption, Peru

Jean-Marie Prival, Jean-Claude Thouret, Saida Japura, Lucia Gurioli, Costanza Bonadonna, Jersy Mariño, Kevin Cueva

▶ **To cite this version:**

Jean-Marie Prival, Jean-Claude Thouret, Saida Japura, Lucia Gurioli, Costanza Bonadonna, et al.. New insights into eruption source parameters of the 1600 CE Huaynaputina Plinian eruption, Peru. Bulletin of Volcanology, 2020, 82 (1), pp.7. 10.1007/s00445-019-1340-7 . hal-02420622

HAL Id: hal-02420622
https://hal.science/hal-02420622

Submitted on 20 Dec 2019

HAL is a multi-disciplinary open access archive for the deposit and dissemination of scientific research documents, whether they are published or not. The documents may come from teaching and research institutions in France or abroad, or from public or private research centers.

L'archive ouverte pluridisciplinaire **HAL**, est destinée au dépôt et à la diffusion de documents scientifiques de niveau recherche, publiés ou non, émanant des établissements d'enseignement et de recherche français ou étrangers, des laboratoires publics ou privés.

New insights into eruption source parameters of the 1600 CE Huaynaputina Plinian eruption, Peru

J.-M. Prival[1], J.-C. Thouret[1], S. Japura[2], L. Gurioli[1], C. Bonadonna[3], J. Mariño[2], K. Cueva[2]

Abstract

In the Central Andes, large Plinian eruptions (Volcanic Explosivity Index ≥ 5) occur at a relatively high frequency, i.e. average of one every 2000 to 4000 years over the past 50,000 years in Peru. Such recurring explosive activity represents a significant challenge for regions typically hosting several million people (e.g. southern Peru, western Bolivia and northern Chile). With VEI 6, the 1600 CE Huaynaputina eruption is considered the largest historical eruption in South America. We have re-examined the first Plinian phase of this eruption in order to better assess critical eruption source parameters (i.e. erupted volume, plume height, mass eruption rate, eruption duration).

The revised bulk volume of the tephra-fall deposit associated with the Plinian phase is approximately 13–14 km^3, almost twice the previous estimate (7–8 km^3 within the 1 cm isopach) based on methods including power law, Weibull function, and Bayesian linear regression. Tephra was dispersed by strong winds to the WNW as far as 400 km on Peruvian territory and then in the Pacific Ocean. Seven villages were buried, killing ~1500 people. The revised plume height estimate, 32.2 ± 2.5 km, is consistent with the early estimations. As a result, the Huaynaputina 1600 CE first eruption phase lies in the upper part of the Plinian field close to the ultra-Plinian transition, making this event one of the largest in the past millennium which coincides with results from recent studies on palaeoclimatic impacts.

Keywords: Tephra-fall deposit • Plume height • Erupted volume • Mass Eruption Rate

[1] Université Clermont Auvergne, CNRS, IRD, OPGC, Laboratoire Magmas et Volcans, F-63000 Clermont-Ferrand, France

[2] Observatorio Vulcanológico del INGEMMET, Barrio Magisterial, Yanahuara, Arequipa, Peru

[3] Department of Earth Sciences, University of Geneva, Geneva, Switzerland

Corresponding author: J.-M. Prival

j-marie.prival@uca.fr

ORCID: 0000-0002-8148-0944

1. Introduction

The study of tephra-fall deposits is fundamental to modern volcanology as they preserve important information about eruption dynamics (e.g. Cas and Wright 1987; Sigurdsson et al. 2015; Bonadonna et al. 2016). Physical characteristics of the deposits such as thickness, grain size, componentry and density are used to estimate critical eruption source parameters (ESPs), e.g. erupted volume (e.g. Pyle 1989; Bonadonna and Houghton 2005; Bonadonna and Costa 2012), plume height (e.g. Carey and Sparks 1986; Burden et al. 2011; Rossi et al. 2019) and mass eruption rate (e.g. Mastin et al. 2009; Wilson and Walker 1987; Degruyter and Bonadonna 2012). Determination of ESPs is essential both for the assessment of volcanic hazards, as they are used as input parameters for tephra dispersal models, and for the characterization and classification of eruptions. The term "Plinian" describes "explosive eruptions characterized by a quasi-steady, hours-long, high speed discharge into the atmosphere of a high-temperature, multiphase mixture (gas, solid, and liquid particles), forming a buoyant vertical column that reaches heights of tens of kilometers" (Cioni et al. 2015). Historical Plinian eruptions include Vesuvius (Italy) in 79, Hatepe (New-Zealand) in 186, Ilopango (El Salvador) in 535, Baekdu (China/North Korea) in 946, Samalas (Indonesia) in 1257, Huaynaputina (Peru) in 1600, Tambora (Indonesia) in 1815, Krakatoa (Indonesia) in 1883, Santa María (Guatemala) in 1902, Novarupta (USA) in 1912, and Pinatubo (Philippines) in 1991 (Sigurdsson et al. 2015, and references therein). Considering the severe and large-scale impacts of these events (Oppenheimer 2011), the volcanology community has put an emphasis on understanding and modelling the dispersal of Plinian tephra (Fagents et al. 2013).

The preservation of tephra-fall deposits is nowhere better than in arid and semi-arid environments such as the Central Andes, where large Plinian eruptions (VEI $\geq$ 6) occur at a relatively high frequency, i.e. on average one every 2000 to 4000 years over the past 50,000 years period in southern Peru (Juvigné et al. 1997, 2008; Thouret et al. 2002b; Sandri et al. 2014). Within the northern segment of the Central Andean Volcanic Zone (CAVZ), as many as seven composite volcanoes erupted in historical times (after the Spanish Conquest in 1540): Ubinas, Sabancaya, Misti, the Andahua-Orcopampa-Huambo monogenetic field, Huaynaputina, Ticsani and Tutupaca (Figure 1). In particular, the 1600 CE Huaynaputina eruption (VEI 6) is considered the largest historical eruption in South America (Thouret et al. 1999, 2002a; Adams et al. 2001) with a major impact on climate. Briffa et al. (1998) have used tree-ring series to estimate a Northern Hemisphere summer anomaly of -0.8 °C in 1601. Stoffel et al. (2015) ranked the year 1601 decrease in temperature as one of the largest volcanic-induced cooling of the Common Era along with Ilopango in 536, Samalas in 1258, Kuwae in 1453, and Tambora in 1816. This cooling had devastating effects not only on the colonial economy in Peru and Bolivia (Figure 2), but at a global scale, from poor wine production in Germany to severe famine in Russia (Verosub and Lippman 2008). Interestingly, no caldera was formed despite the high volume of tephra emitted, although ring fractures are observed across the remaining crater (Lavallée et al. 2006). Given the accuracy of hazard assessment of volcanic eruptions is based on the accuracy of associated ESPs, we have re-examined the Plinian phase of the 1600 CE Huaynaputina eruption applying the most recent strategies in order to better assess erupted volume and plume height. This phase emplaced a massive tephra-fall deposit with 70–80 % pumice, 15–25 % free crystals and ~5 % lithic clasts (Thouret et al. 2002a).

Previous studies of the 1600 CE Huaynaputina eruption were carried out between 1999 and 2002 (Thouret et al. 1999, 2002a; Adams et al. 2001). In the past decade, both the characterization of tephra-fall deposits and the determination of ESPs have considerably evolved (see Bonadonna et al. 2015 for a review). Our revision of the dataset in 2015–2017 was motivated by the application of recent models in order to better assess erupted volume, plume height, mass eruption rate (MER) and eruption duration. In particular, the estimation of erupted volume was based on the models of Bonadonna and Houghton (2005), Bonadonna and Costa (2012) and Burden et al. (2013). Plume height was determined using the method of Bonadonna and Costa (2013), Biass et al. (2015) implementation of Carey and Sparks (1986), and Rossi et al. (2019). MER was determined based on the methods of Wilson and Walker (1987), Mastin et al. (2009), and Degruyter and Bonadonna (2012). Eruption duration was derived based on all combinations of erupted mass and MER. The TError package (Biass et al. 2014) was also applied to investigate uncertainty propagation through the calculation of ESPs. Finally, the eruption was also classified based on the scheme of Bonadonna and Costa (2013).

2. Geological and volcanological setting

2.1. CAVZ and Holocene explosive volcanism in southern Peru

The Central Andean Volcanic Zone is a 1500 km long volcanic arc extending from southern Peru to northern Chile (Figure 1). The CAVZ results from the subduction of the Nazca plate under the South American plate, with a present-day convergence rate of 64 mm/yr (Norabuena et al. 1999). The arc volcanism is characterized by large silicic systems producing andesitic, dacitic and rhyolitic magmas (Rivera et al. 2017). This suite has long been interpreted as the result of assimilation and fractional crystallisation of basaltic magma during its ascent through the > 65 km thick Central Andean crust (Thorpe 1984; Wilson 1989).

The CAVZ silicic systems have produced large (VEI 5–6) explosive eruptions, including caldera forming events, during the Holocene. Examples of this activity include Misti, with pumice-fall as recent as c. 2070 yr BP, c. 3800 yr BP, and c. 5200 yr BP (Thouret et al. 2001; Cobeñas et al. 2012), and Ubinas as recently as c. 980 yr BP (Thouret et al. 2005). The most recent Plinian eruption, and by far the largest historical event in South America, occurred in February-March 1600 at Huaynaputina, approximately 75 km east of the city of Arequipa. The CAVZ explosive activity poses a great challenge to south Peru, a region now hosting two to three million people.

2.2. Huaynaputina volcano

Despite its stratovolcano status in catalogues (Siebert et al. 2010), Huaynaputina is not a “classical” cone-shaped edifice. With the summit ridge elevation at 4860 m a.s.l., it lies only a few hundred meters above the surrounding high plateau made of Cretaceous sediments, Paleogene volcaniclastics, and Neogene lava flows and ignimbrites. Huaynaputina was a dome cluster built up over a Pleistocene composite volcano whose low angle-dipping lava flows are still visible across the scar of a flank failure towards the Río Tambo canyon, cut down 2.6 km deeper on the east flank of the plateau. Inside the 2.5 km wide horseshoe-shaped scar of the flank failure, the 1600 CE eruption formed three nested craters cut by ring fractures (Figure 3). The 1600

eruption destroyed the lava domes and pre-existing deposits that crop out in the amphitheatre rim, while one large, compound dome (Cerro Volcán) remained 3 km south of the craters (Figure 3). Hanging valleys, cut by the amphitheatre scar, were filled by block-and-ash-flow deposits bearing witness to the pre-existing dome clusters atop the stratovolcano. A Plinian tephra-fall deposit found in Laguna Salinas (35 km from the volcano) and dated at 9700 ± 190 years BP may be attributed to Huaynaputina (Juvigné et al. 1997). This deposit also crops out along the valley of Río Tambo (Pampa Yamure) 6−7 km east of Huaynaputina beneath the 1600 CE tephra-fall deposit.

2.3. The Plinian tephra-fall deposit of the 1600 CE eruption

Field studies have been used to reconstruct the 1600 CE eruption of Huaynaputina (Thouret et al. 1999, 2002a; Adams et al. 2001). Adams et al. (2001) have identified three units, while Thouret et al. (2002a) distinguished five main units and correlated them with data from a wealth of early Spanish chronicles (Table 1 in Thouret et al. 2002a). New field data acquired in 2017 further confirms the existence of five eruptive units, including sections located 60 km WNW of the crater (e.g. Yarabamba section, Figure 4b). These units are: (1) A Plinian tephra-fall deposit; (2) A sequence of mm and cm-thick ash layers, interpreted as post-Plinian ashfalls; (3) Several non-welded ignimbrites, cropping out in valleys around the vent, corresponding to a phase of pyroclastic flows; (4) A crystal-rich (up to ~80 % free crystals) ashfall deposit; (5) Small volume ash flow deposits. In this work we focus on the first one, i.e. the Plinian tephra-fall deposit, referred to as “Unit 1” in the remainder of this paper, as it is the most significant volumetrically (62–67 % of the total volume, Thouret et al. 2002a).

The description of Unit 1 (Figure 5) is based on the “Quinistacas Football Club” section (QFC) located 12.5 km WSW of the craters. The QFC section shows seven subunits within Unit 1. Despite the very coarse grain size nature (few decimetre-sized pumice) and tightly packed pumice-fall deposit, as many as five subunits have also been distinguished throughout the 11-m thick section near the top of the flank failure scar, 0.5 km west from the vent area. During field work, we have measured thickness, density and grain-size for each subunit to check for potential vertical variations. However, for simplicity of the models, in this article we consider the total thickness of Unit 1, and its average density (see methods).

3. Methods

3.1. Thickness, grain-size and density measurements in the field

Arid to semi-arid field conditions, and the quality of outcrops preserved around Huaynaputina and along the dispersal axis, make this tephra-fall deposit a unique reference for such a voluminous Plinian eruption, although part of the tephra fell into the ocean (~39 % of the 1 cm isopach area covers the Pacific Ocean, calculated with QGIS). The extent and thickness of Unit 1 has been investigated throughout extensive field work between 1995 and 2000. Peat bogs have been cored in marshes and small lakes to retrieve the deposit in distal areas (Juvigné et al. 1997).

Additional fieldwork has been carried out in 2015–2018 in the framework of the Huayruro Project (http://ovi.ingemmet.gob.pe/?tag=proyecto-huayruro), expanding the dataset with 42 new sections in

proximal and medial areas. Following Bonadonna et al. (2013), grain-size was determined as the 50th percentile of the geometric mean of the three axes of the 20 largest clasts. These clasts are spread over a ~6000 km^2 area around the vent. Bulk density of Unit 1 was measured using plastic tubes to collect tephra samples, including coarse pumices but avoiding breaking them in the process. We collected one tube per subunit as distinguished throughout the tephra section (at least two layers in distal sections to as many as six layers in proximal sections, Table S1). We dried the samples at ~70 °C for 24 hours in a small oven available in a village nearby and weighed them with an electronic weigh scale (0.1 g) to obtain the dry mass. Dry bulk density was calculated as the ratio between the mass and the volume of the tube. The whole deposit density was calculated as the mean of the densities weighted by their respective subunit thicknesses.

3.2. Tephra-fall deposit volume

To determine the volume of tephra of Unit 1, both Adams et al. (2001) and Thouret et al. (1999, 2002a) used the exponential method of Pyle (1989) modified by Fierstein and Nathenson (1992). Based on the observations made on Mount Hekla by Thorarinsson (1954), the method assumes that tephra-fall deposit thickness decreases exponentially with distance from the vent. Thus, field data should usually show a linear trend in a semi-log plot of thickness vs. square root of isopach area. The straight-line segment equation is:

$$T = T_0 \exp\left(-k\sqrt{A}\right) \qquad (1)$$

where A is the area of isopach contour of thickness T, k the slope of the segment, and T_0 the extrapolated maximum thickness. Pyle (1989) integrated Eq. 1 to compute the volume of tephra encompassed by the minimum thickness isopach contour. Bonadonna et al. (1998) have shown that the exponential method can significantly underestimate the volume of tephra when applied to poorly exposed deposits as it cannot well reproduce the natural gradual thinning. Two statistical methods have since been developed to better model this trend: one with a power-law (Bonadonna and Houghton 2005) and one with a Weibull function (Bonadonna and Costa 2012). According to the power-law fitting, tephra thickness decreases with respect to distance from vent as:

$$T = T_{pl}\sqrt{A}^{(-m)} \qquad (2)$$

where T_{pl} is the power-law coefficient and m the power-law exponent. Given that Eq. 2 cannot be integrated between zero and infinity, the proximal (B) and distal (C) integration limits have to be defined in order to estimate the volume:

$$V = \frac{2T_{pl}}{2-m}\left(C^{(2-m)} - B^{(2-m)}\right) \qquad (3)$$

B can be determined based on the extrapolation of the first exponential segment (Bonadonna and Houghton 2005). The determination of C, however, is more complex. The maximum value of C was determined in association with a thickness value of 1 mm (~2100 km in square root of area). It is important to note that for this Unit, m is < 2 (typical of large eruptions or poorly exposed deposits), therefore the volume is sensitive to the choice of C.

Similarly, the Weibull function can fit the decrease of thickness with the following relationship:

$$T = \theta_{th}\left(\frac{\sqrt{A}}{\lambda_{th}}\right)^{n_{th}-2}\exp\left[-\left(\frac{\sqrt{A}}{\lambda_{th}}\right)^{n_{th}}\right] \qquad (4)$$

where θ_{th} , λ_{th} and n_{th} are the Weibull parameters of the fit. Equation 4 is used to express the volume as a function of $\sqrt{A}$. This expression is then integrated between zero and infinity to obtain the total volume:

$$V = \frac{2\theta_{th}\lambda_{th}^2}{n_{th}} \qquad (5)$$

In case of well-exposed deposits, the integration of the Weibull fitting represents a good compromise between the exponential and the power-law strategy as it can better reproduce the thinning of the deposit with respect to the exponential method, and it can be integrated between zero and infinity.

Burden et al. (2013) have proposed a statistical approach to determine the volume of a deposit directly from the real thickness measurements in order to bypass the uncertainty associated with the compilation of isopach maps. The authors consider that a scatter plot of ln(thickness) vs. distance from the vent is characterized by a trend that can be fitted by a linear regression:

$$z_i = \alpha + \beta d_i + \varepsilon_i \qquad (6)$$

where z_i is the natural logarithm of thickness measurement y_i, located at a distance d_i from the vent. α stands for the modelled thickness at the vent, β the decrease of thickness with distance (thus $\beta > 0$). The error term ε_i is normally distributed with a variance of σ^2. Assuming that the deposit is isotropic (i.e. the thickness does not depend on direction), its volume is expressed as:

$$V(\alpha,\beta) = \int_0^{\exp(\alpha)} \pi\left(\frac{\ln(y)-\alpha}{\beta}\right)^2 dy \qquad (7)$$

Bayesian linear regression is used to determine the posterior probability density function for α, β and σ^2. This distribution is then used to generate samples of α, β and σ^2 with a Markov chain Monte Carlo method. According to Burden et al. (2013), ten thousand samples are enough to reach convergence, i.e. a good approximation of the target distribution. A distribution of 10,000 predicted volumes is calculated by using these samples in Eq. 7. The volume is then expressed as the median of the distribution.

3.3. Plume height

We have used three methods to determine the maximum height *H* reached by the plume. As the dataset has been revised with additional data acquired with an improved strategy, we re-calculated *H* following Carey and Sparks (1986). The method is based on a model of clast fallout from a convective column, in which clast dispersal is determined by two main parameters: column height and wind speed. This method presents two shortcomings: (1) the user needs to plot the data "by hand" on the diagram, which can lead to some inaccuracy; and (2) one diagram alone cannot encompass all clast sizes at a time. We have applied the MatLab implementation of the method proposed by Biass et al. (2015). This implementation interpolates Carey and Sparks (1986) diagrams to a continuous range of clast sizes and provides well-defined plume height and wind speed estimates.

The method of Bonadonna and Costa (2013) also relies on the relationship between the size of the maximum lithic clasts (ML) and the distance from the vent. The resulting empirical relation is:

$$H\ (\text{km}) = 5.01\lambda_{ML}^{0.55} \qquad (8)$$

with a typical error of 10–15 % and a maximum error of 25 %. We determined the Weibull parameters of the revised Huaynaputina isopleth data by minimising the sum of squared relative residuals in a semi-log plot of ML vs. *x*. The plume height was then calculated with Eq. 8.

Finally, we applied the recent model of Rossi et al. (2019), which accounts for the interaction of plume and wind. This new strategy refines both the definition of the clast support envelope, by accounting for the effect of wind advection on a rising plume, and the determination of particle trajectories, by integrating the drag force to the sedimentation equation. By introducing a drag coefficient, this model accounts for the effect of particle shape on settling velocity.

3.4. Mass eruption rate and eruption duration

Three methods were used to determine the mass eruption rate (MER):

(1) Wilson and Walker (1987). This method relates MER to the maximum plume height *H* with the empirical relation:

$$MER = \left(\frac{H}{k}\right)^4 \qquad (9)$$

where *k* is a constant depending on the magma's chemistry. In this study we used 0.236, the typical value for silicic magmas.

(2) Mastin et al. (2009). It is based on the best fit between the volumetric flow rate $\dot{V}$ (m^3 DRE per second) with maximum plume height *H*, calculated on a database of ~30 eruptions:

$$\dot{V} = \left(\frac{H}{k}\right)^{4.15} \qquad (10)$$

where *k* is a constant set to 2. Knowing the DRE density of the magma, the volumetric flow rate can then be converted to MER.

(3) Degruyter and Bonadonna (2012) developed a new expression considering the wind:

$$MER = \pi\frac{\rho_{a0}}{g'}\left(\frac{\alpha^2\overline{N}}{10.9}H^4 + \frac{\beta^2\overline{N}^2\bar{v}}{6}H^3\right) \qquad (11)$$

where ρ_{a0} is the reference density of the surrounding atmosphere (kg m^{-3}), g' is measured in m s^{-2} and defined as $g \cdot \left((c_0\theta_0 - c_{a0}\theta_{a0})/c_{a0}\theta_{a0}\right)$ with g being the gravitational acceleration, α is the radial entrainment coefficient, $\overline{N}$ is the average buoyancy frequency (s^{-1}), *H* is the plume height above the vent (m), β is the wind entrainment coefficient, and $\bar{v}$ is the average wind velocity across the plume (m s^{-1}).

MER estimates were then used to calculate the eruption minimum duration with all volume estimates (converted to mass).

3.5. Uncertainty of eruption source parameters

To assess the uncertainty of the revised ESPs' estimates, we used TError (Biass et al. 2014), a package of Matlab functions that handles various methods applied to several ESPs, namely:

– Plume height and wind speed, after Carey and Sparks (1986).

– Mass eruption rate, after Wilson and Walker (1987), Mastin et al. (2009) and Degruyter and Bonadonna (2012).

– Tephra volume, after Fierstein and Nathenson (1992), Bonadonna and Houghton (2005) and Bonadonna and Costa (2012). Mass is then determined using a constant bulk deposit density.

– Duration, calculated as the ratio between mass and MER.

For each input parameter, the user chooses a reference value and a relative input uncertainty (RIU), for instance ± 10 %. TError then runs Monte Carlo simulations to generate uncertainty distributions, symmetrical and centred around the reference value (considered as the best possible guess). Due to the absence of studies on the shape of such distributions, the authors decided to implement both normal and uniform distributions. Input parameter distributions are used to produce probability distributions of ESPs. An ESP is subsequently expressed as the mean of its distribution while the lower and upper boundaries can be defined by chosen percentiles. In this study, we chose to apply a 20 % RIU on all input parameters, to use a normal distribution, and to run 10,000 Monte Carlo simulations arguing that Biass et al. (2014) showed that results were stable beyond that number.

3.6. Eruption classification

Walker (1973) proposed the first quantitative classification scheme of explosive volcanic eruptions based on the area of dispersal (D) vs. degree of fragmentation (F) to define four eruption styles: Hawaiian / Strombolian (low D, low F); Plinian (high D, low F); an intermediate sub-Plinian category between the first two; and Surtseyan (low D, high F). However, this method requires sieving grain size data from a specific location, which is not always available. Pyle (1989) also pointed out that F does not necessarily reflect total magma fragmentation but is "clearly strongly influenced by depositional processes" (e.g. aggregation) instead. Pyle's classification scheme introduced two quantitative parameters. The first one is *bt*, "the distance over which the thickness halves", defined as $bt = \ln(2)/k$, where k is the slope of the segment on a semi-log plot of thickness vs. (isopach area)$^{1/2}$. The second parameter is the maximum clast half-distance, $bc = \ln(2)/k_1$, where k_1 is the slope of the segment on a semi-log plot of grain size vs. (isopleth area)$^{1/2}$. The parameter *bt* represents dispersal, while *bc* is linked to plume height by an empirical relationship. In his classification scheme, Pyle plotted *bc/bt* vs. *bt* and chose integer values of *bc* as boundaries between eruptions styles. The main drawback of the method is that if the isopach (or isopleth) semi-log plot presents several segments, which result in several values of *bt* (or *bc*). A single event can thus be represented by multiple points on the *bc/bt* vs. *bt* classification plot. This is the case of the 1600 CE Huaynaputina eruption (Fig. 10A and 10B in Thouret et al. 2002a).

Explosive volcanic eruptions can also be classified based on the Weibull description of both deposit thickness and distribution of the largest clasts (Bonadonna and Costa 2013). This classification scheme

removes the ambiguous choice of *bt* and *bc* as the Weibull parameters (λ_{th} and λ_{ML}) are unique for a given deposit. We applied it to Unit 1.

4. Results

4.1. Thickness, grain-size and density of the deposit

Including the 42 new sections, the dataset currently encompasses over 600 thickness measurements, which have been compiled with a GIS to build a revised isopach map (Figure 6). The dispersal axis is oriented WNW (the proximal WSW orientation is probably biased by the distribution of points). The ML isopleth map has also been revised (Figure 7). This distribution is characterized by a West elongation pattern. Finally, dry bulk density of each subunit of the Plinian tephra-fall deposit has been measured in 32 sites. It slightly increases between proximal, medial and distal tephra sections, but it does vary from base to top across tephra sections. The dry bulk density of Unit 1 rises with distance from the vent, with a mean of 0.62 g/cm^3 for proximal deposits and 0.72 for distal deposits (Figure 8a, Table S1). The density also varies vertically across subunits (Figure 8b), with the uppermost, thin lithic-rich layer being the densest.

4.2. Volume estimates

Table 1 summarizes the results obtained with the four volume estimation methods, namely exponential (Bonadonna and Houghton 2005), power law (Bonadonna and Houghton 2005), Weibull (Bonadonna and Costa 2012), and Bayesian linear regression (Burden et al. 2013), along with their respective parameters. Figures Figure ***9*** and Figure ***10*** shows the corresponding plots, where the exponential segment shows the best fit (i.e. is associated with the lowest sum of squared relative residuals). It is important to note that even though the exponential fit is characterized by the lowest sum of squared relative residuals, it does not mean that the last exponential segment better extrapolates the data. The discrepancy between models is reflected in volume estimates, with a Weibull-based result almost twice as much as the exponential-based result.

4.3. Plume height estimates

Table 2 shows the result of Biass et al. (2015) implementation of Carey and Sparks (1986) method for four isopleths ranging from 1 to 5 cm, along with Rossi et al. (2019) model. Wind speed estimates are consistent with what is observed nowadays above the tropopause in South Peru. We processed the NCEP/NCAR reanalysis 1 dataset (Kalnay et al. 1996) with TephraProb (Biass et al. 2016). In February, the median wind speed reaches approximately 20 m s^{-1} at 20 km of altitude, and increases up to 35 m s^{-1} at 30 km. From 20 km upwards, the wind orientation is almost constant at 270°, i.e. blowing towards the West, which matches the dispersal axis of 1600 CE Huaynaputina Plinian tephra-fall deposit (Figure 6). Figure Figure ***11*** shows the Weibull fit of isopleth data. The corresponding parameter λ_{ML} yields a plume height of 33.5 km calculated with Eq. 8. Adams et al. (2001) and Thouret et al. (2002a) found similar values of ~34 km and ~33 km, respectively, applying Carey and Sparks (1986) model.

4.4. Mass eruption rate and eruption duration

MER estimates vary with a factor of two, from 1.4 × 10^8 kg/s (Mastin et al. 2009) to 3.2 × 10^8 kg/s (Degruyter and Bonadonna 2012). Wilson and Walker (1987) method yields an intermediate value (2 × 10^8 kg/s). Thouret et al. (2002a) found 1.3–1.6 × 10^8 kg/s using the Sparks (1986) method. Combined with our four volume estimates (converted to mass), these MERs give twelve minimum durations ranging between 5 and 19 hours. This interval is consistent with the 12–19 hours estimate based on the analysis of Spanish chronicles. Depending on the MER estimate, the eruption intensity (as defined by Walker 1980) ranges from 10.8 to 11.6.

4.5. Uncertainty propagation in eruption source parameters

We have used the TError package to assess the uncertainty associated with our ESPs estimates. Table S2 summarises a TError run after 10,000 iterations, with a 20 % relative input uncertainty normally distributed. This normal distribution can propagate in the output parameter when the input–output relationship is linear. This is the case of the plume height, for instance, which can thus be expressed with a single error range, i.e. 32.2 ± 2.5 km. Non-linear relationships yield asymmetric ESP distributions, like the case of volume estimated with the Weibull function. The volume should therefore be expressed as 14^{+1}_{-3} km^3, with both the lower and upper errors mentioned.

4.6. Classification

To compare the 1600 CE Huaynaputina pumice tephra-fall deposit with that of other explosive events, we plotted the data in Bonadonna and Costa (2013) Weibull classification scheme (Figure 12). The eruption plots in the Plinian field, within the lower 20 % of the Plinian–ultra-Plinian boundary. The deposit has a larger λ_{th} than any other eruption for which this parameter has been calculated. This is an indication of a gradual thinning, which is probably better described for this unit due to the large amount of field observations. Nevertheless, the Huaynaputina eruption ranks among the largest Plinian events of the Common Era, a fact corroborated by Stoffel et al. (2015).

5. Discussion

The re-analysis of the Huaynaputina case has led us to discuss the evolution of tephra studies, from sampling strategy to ESP estimates and eruption reconstruction. The following section discusses limitations on modelling along with some perspective for future work.

5.1. Volume estimation methods

The integration of the exponential best-fit, even if based on 4 exponential segments, likely underestimates the volume of Unit 1 (8.2 km^3) as it cannot well describe the distal thinning associated with particle sedimentation in the laminar regime. The integration of the power-law best-fit for the calculation of tephra-fall deposit volume (13.3 km^3) requires careful selection of integration limits, which, in particular for the case when the power-law exponent is < 2, can result in large uncertainties in the volume estimate. A

± 500 km uncertainty on the integration limit result in a ± 2.3 km^3 variation on the volume estimate (about 17 % of the total volume). The Weibull function and the Bayesian linear regression yields similar volume estimates (14.4 and 14.3 km^3, respectively). Burden et al. (2013) found a good correlation with previously determined volumes for four out of five case studies. Our result provides additional evidence in favour of the method. However, it can fail to predict the thickness at the source. In the Huaynaputina case, it predicts 27 cm, entirely at odds with the 11–12 m actually observed on the amphitheatre rim. The reason is that the coexistence of high thickness values (downwind) and low thickness values (upwind) at the same distance from the source interferes with the trend.

It is important to note that, regardless of the resulting volume estimate, all models provide important insights into tephra sedimentation. For instance, the breaks-in-slope between exponential segments reflect the transition amongst sedimentation regimes processes (Bonadonna et al. 1998; Bonadonna and Phillips 2003). Based on the theoretical relation proposed by Bonadonna and Phillips (2003), we can infer that the plume corner was between 5-6 km and 6-7 from the vent depending on the values for plume height (26-30 km with the model of Rossi et al. 2019 and 32-35 km with the model of Carey and Sparks 1986). We can conclude that the first break-in-slope (4 km from vent) is consistent with the transition between sedimentation from plume margins and sedimentation from the umbrella cloud, while the other two breaks-in-slope (28 km and 69 km from vent) indicate the transition between turbulent and intermediate regime and intermediate and laminar regime of sedimentation, respectively. The presence of three breaks-in-slopes consistent with particle-sedimentation dynamics indicates that the thinning trend shown in Figure 9 is representative of most of the original tephra-fall deposit.

The fact that three methods converge towards a 13–14 km^3 volume of tephra leads us to reconsider the previous results of 7 km^3 (Adams et al. 2001) and 8 km^3 (Thouret et al. 2002a), which did not consider tephra deposited beyond the 1 cm isopach. In fact, the revised volume estimate of 13–14 km^3 should be considered as a minimum because the distal deposit has likely been removed while the remaining deposits in proximal and medial areas has been compacted, which can lead to a 40 % volume decrease (Thorarinsson 1954). In addition, and despite the fact that Unit 1 is now well constrained in the proximal and medial areas, a significant amount of tephra drifted to the Pacific Ocean and will never be quantified accurately. The closest drilling core from the International Ocean Discovery Program (site 1237) records 55 layers of andesitic ash since 9 Ma (Mix et al., 2003). However, the shallowest ash layer (at 6 m in depth) is likely too old to correspond to the 1600 CE eruption of Huaynaputina.

According to Biass et al. (2014), three categories of uncertainty are inherently associated to the construction of isopach maps: (1) some natural processes, such as erosion and compaction, can alter the deposit; (2) measuring techniques for tephra studies are not standardized, although substantial progress has been made in recent years (Bonadonna et al. 2011, Bonadonna et al. 2015); (3) subjective choices are being made when hand-drawing contour lines (Klawonn et al. 2014). The first uncertainty is impossible to overcome−except in rare cases where the deposit is preserved in peat bogs–but the last two can be reduced. Recent works allow us to rule out the subjectivity of hand-drawn maps by calculating deposit volumes directly from thickness data. Engwell et al. (2015) method defines objective isopach contours using cubic B-

spline interpolation of thickness data. Once the isopachs are built, the volume of the deposit can be calculated by integration of the cubic B-spline surface. One advantage of the method is that each data point can be weighted individually to account for thickness measurements uncertainty. Yang and Bursik (2016) proposed to model tephra thickness though detrending and kriging. They consider that tephra thickness is the sum of a general trend and local variations that could have a physical meaning ("inhomogeneities in source conditions, or turbulence structures that drive the transport of tephra"), and should thus be modelled. Kriging is used to predict the value of a random variable (here thickness) based on the observed data, providing a grid with an interpolated thickness value attached to each cell. The total volume of tephra is then calculated by summing the volume of each cell with a simple pixel-by-pixel strategy.

5.2. Plume height and dynamics

When the 1600 CE Huaynaputina eruption was first investigated in the late nineties, sampling strategies were not yet standardised. Thouret et al. (2002a) determined maximum pumices and lithics by calculating the algebraic mean of three axes of the 10 largest clasts (after Suzuki et al. 1973). Adams et al. (2001) used the long axes average of three to five clasts. The IAVCEI Commission on Tephra Hazard Modelling currently recommends computing the 50th percentile of the geometric mean of the three axes (Bonadonna et al. 2013) of the 20 largest clasts. However, Osman et al. (2019) have also shown how, while the 50th percentile of 20 clasts provide the best results at the scale of the outcrop, the average of the geometric mean of the 5 largest clasts is best comparable with the method of Carey and Sparks (1986). We applied the new strategy during the most recent field campaigns in 2015–2017: the revised ML values have not changed much but MP estimates have been modified. In any case, ML values are those considered in our calculations as lithics are preferred for plume height estimates. MP values are less critical because pumices tend to break when impacting the ground (Walker 1980).

It is important to note also that accounting for wind advection on plume rise (i.e. model of Rossi et al. 2019) results in lower plume heights with respect to those predicted by the model of Carey and Sparks (1986) (Table 2). In fact, allowing the plume to bend due to the wind enables a more accurate correlation between height of release and sedimentation of clasts. The values of plume height obtained with the model of Rossi et al. (2019) are also consistent with the independent results obtained on the regimes of particle fallout in relation to the position of breaks-in-slope shown by the tephra-deposit thinning discussed in previous section (Figure 9).

The eruption duration, one key parameter, remains a challenge. It appears impossible to better constrain than the estimated 12–19 hours duration based on Spanish chronicles (Thouret et al. 2002a). This ~50 % uncertainty propagates into mass eruption rate and intensity calculations. Methods computing MER from plume height can be used to derive duration; in the Huaynaputina case study, considering the 13–14 km^3 as the best volume estimate, the Wilson and Walker (1987) method yields a duration estimate close to the chronicles, i.e. ~13 hours (~18 hours with Mastin et al. 2009, ~8 hours with Degruyter and Bonadonna 2012, Table S2).

Relating deposit features to plume dynamics may be challenging. Deposit stratification can be explained by changes in mass eruption rate, generating an oscillating column.

5.3. Potential impacts in South Peru from a future Plinian with same intensity, magnitude and wind dispersal as the Huaynaputina event

If we consider the area affected by the Huaynaputina Plinian eruption in 1600, the impacts of a future large scale (VEI 6), explosive eruption would be catastrophic. The area impacted by the 1600 eruption–128,000 km^2 within the 1 cm isopach, and over 400,000 km^2 within the 1 mm isopach–now hosts one fourth of Peru's population, i.e. about 8 million inhabitants (all socioeconomic data presented here are from the Peruvian Institute of Statistics and Data Processing, INEI). Eight among the Peru's 24 departments were, and can be affected: Arequipa, Moquegua, Tacna, Puno, Cusco, Ayacucho, Apurimac and Ica. In addition, ash fallout was also reported in west Bolivia and north Chile. Both neighbouring countries can be affected by tephra fallout from at least one of the Peru's historically active volcanoes. Unrest is now (2018) reported at Misti and Ticsani, while Sabancaya (since 2016) and Ubinas (since 2013) are sporadically erupting, albeit mildly.

Impacts can include fatalities, damage to building and critical infrastructures, such as road, water and electricity networks, and important activities such as agriculture, mining, fishing, cattle breeding and tourism (Jenkins et al. 2015, Figure 13). Two areas must be considered:

(1) The proximal zone (within 25 km from the vent) which covers 1500 to 1900 km^2 and now hosts about 90,000 people (1000 people were reported missing after the 1600 eruption according to Navarro 1994). The proximal zone cannot be easily evacuated as most of the road network around Huaynaputina consists of dirt roads (although roads are being paved over the past two years). To worsen the situation, most of the main roads, which are unpaved so far, are in close range of active volcanoes Ubinas and Tiscani, while bridges over the principal rivers (e.g. Río Tambo, Chili, Vitor, and Majes) are scarce, narrow and vulnerable to lahars. The destruction would be complete or severe in this zone covered by thick (> 1 m) tephra, on slopes swept by PDCs, and along valleys conveying lahars. Lahars that swept the Río Tambo canyon reached the Pacific coast, 120 km away (Thouret et al. 2002a).

(2) The medial zone (within 120 km from the vent) includes the Arequipa and Moquegua departments, and may include the Puno department depending on the ash dispersal direction. This represents about 3 million people who would temporarily suffer from health problems and whose transportation would be disrupted. If the Plinian eruption were to encompass an area as large as the 1600 isopach area, we consider that as many as 9 to 12 million people (including tourists in south Peru, west Bolivia and north Chile) would be affected.

South Peru hosts two large, business and touristic centres: Arequipa and Cusco. Arequipa, Peru's second largest city and a UNESCO World Heritage site, hosts at least 0.9 million people (INEI data as of 2012), to which 435,000 in Cusco, 320,000 in Tacna, and 120,000 in Puno must be added, not to mention 30,000 to 70,000 people in each of the smaller cities (e.g., Camana, Mollendo, Ilo, Juliaca, Caraveli). Agriculture, breeding of camelids, and mining activities would suffer more from any large (> VEI 5) Plinian eruption, particularly camelid breeding in mountain environment, irrigation networks on slopes, as well as irrigated meadows and crops located in special irrigation projects that have been developed over the past 30

years along the wide river plains (Rio Majes, Vitor, Tambo, Moquegua), all flood prone in case of lahars. Mining activities, which rank second after fishing and represent 17 to 21 % of Peru's GDP, would be interrupted, and indirect loss (including unemployment and decrease in GDP) could reach dramatic proportions nationwide. Fishing would be affected along the 500-km long coast of south Peru together with dire consequences on employment and food supply nationwide. In addition, a majority of the 3.5 million of tourists who visit Peru each year (touring especially Arequipa, Cusco and Puno–Lake Titicaca) could not travel to the affected zone. Tourism, the third most important source of income in Peru, has increased annually by 5 % as the conditions have improved since around 2010. Transportation would be interrupted, especially the airports. The Arequipa airport is the country's third-largest hub after Lima and Cusco in terms of passengers. Other important airports of the region such as Tacna and Juliaca would be affected, as would railways towards Cusco and La Paz. Transportation to large mines in south Peru (copper in Cerro Verde and Cuajone; gold and silver in the Arequipa, Ayacucho, and Apurimac departments) could be interrupted, while the the Transoceánica road to the sea, which is the only exit for Bolivian equipment and goods, could be closed. This paved road, winding up within 40 km of the Huyanaputina vent and 12 km from the Ticsani domes, links La Paz to the harbor of Ilo (67,000 inhabitants, located 125 km SW of Huaynaputina) near Moquegua. In addition, transportation and exchanges would be stopped between north Chile (Arica, a city of 155,000 inhabitants 205 km south of Huaynaputina), west Bolivia (Deasaguadero and La Paz, 2.3 million inhabitants 290 km east of the volcano) and Peru.

In sum, we estimate the dramatic decrease in Peru's GDP, heavily based on mining, fishing, agriculture, trade and tourism activities, to be in the range of 10 to 20 % annually, if the mid and long-term economic impacts of large explosive eruptions in similar developing countries (Pinatubo in 1991, Fuego in 2018) are accounted for.

Conclusion

The 1600 CE Huaynaputina eruption had first been studied in 1999–2002. Analysis of tephra-fall deposits has since evolved using both detailed field and laboratory studies. With this analytical progress in mind, we reconsidered the case study in 2015–2017, focusing on the first of the five phases of the eruption, i.e. the Plinian explosive event of 19 and 20 February 1600. This research consisted of two stages: (1) we revised the previous datasets, compiling all thickness and largest-clast data and adding bulk deposit density measurements; (2) we applied recent methods to estimate eruption source parameters (volume, plume height, MER) and the associated uncertainty. The key findings in terms of eruption dynamics are as follows:

1. The Plinian phase likely dispersed tephra WNW beyond 400 km from the vent over the Peruvian territory and the Pacific Ocean. This gradual thinning trend can be extrapolated by modern techniques to account for this missing volume of tephra. Three volume estimation methods (power law, Weibull function, Bayesian linear regression) provide a similar result in the 13–14 km^3 range, leading us to revise the previous 7–8 km^3 estimates of Adams et al. (2001) and Thouret et al. (2002a) based on the exponential method (Pyle, 1989). This ranks the eruption among the largest Plinian events of the Common Era in the world.

2. The tephra plume reached a maximum altitude of 26–31 km and drifted to the WNW by strong winds. This estimate is lower than previous estimates (~33 km by Thouret et al. 2002a, ~34 km by Adam et al. 2001) because they did not account for wind advection in the plume.

As for methodology used in tephra studies, this work has highlighted that:

1. In order to reduce the uncertainty associated with ESPs, volcanologists must follow standard, well-defined strategies when collecting data. This also allows the scientific community to compare eruptive events.
2. Quantifying the uncertainty in eruption source parameters estimates is crucial. This can be achieved by assessing the uncertainty associated with field observations and investigation of the uncertainty propagation into ESP distributions. These distributions can then be used to state the confidence interval of the estimate.

In the CAVZ and arguably across the Andes, where Plinian events are relatively frequent, an accurate characterization of tephra-fall deposits is crucial to assess the hazards and potential impact on the populations of Peru, Bolivia and Chile.

Acknowledgments

The authors thank Sébastien Biass for his help with TError and Qingyuan Yang for pointing out some errors in an early version of the dataset. Associate Editor Marcus I Bursik, Stephen C Kuehn and an anonymous reviewer are thanked for their thorough reviews of the manuscript. This is Laboratory of Excellence ClerVolc contribution n° 377.

Funding information

Field work was funded by a Institut de Recherche pour le Développement – Laboratoire Magmas et Volcans program on recent and active volcanism in south Peru, through cooperation between the Instituto Geológico, Minero y Metalúrgico (Peru) and study abroad office at Université Clermont Auvergne (France), and through the Huayruro project, funded by the Fondo National de Desarrollo Científico y Tecnológico. A trip to Université de Genève to work with Costanza Bonadonna was funded by the Observatoire de Physique du Globe de Clermont-Ferrand. Costanza Bonadonna was funded by the Swiss National Science Foundation (#200021_163152).

References

Adams N, de Silva S, Self S, Salas G, Schubring S, Permenter J, Arbesman K (2001) The physical volcanology of the 1600 eruption of Huaynaputina, southern Peru. Bull Volcanol 62:493–518. https://doi.org/10.1007/s004450000105

Biass S, Bagheri G, Aeberhard W, Bonadonna C (2014) TError: towards a better quantification of the uncertainty propagated during the characterization of tephra deposits. Stat Volcanol 1:1–27. https://doi.org/10.5038/2163-338X.1.2

Biass S, Bagheri G, Bonadonna C (2015) A matlab implementation of the Carey and Sparks (1986) model. URL https://vhub.org/resources/3922

Biass S, Bonadonna C, Connor L, Connor C (2016) TephraProb: a Matlab package for probabilistic hazard assessments of tephra fallout. J Appl Volcanol 5. https://doi.org/10.1186/s13617-016-0050-5

Bonadonna C, Biass S, Costa A (2015) Physical characterization of explosive volcanic eruptions based on tephra deposits: Propagation of uncertainties and sensitivity analysis. J Volcanol Geotherm Res 296:80–100. https://doi.org/10.1016/j.jvolgeores.2015.03.009

Bonadonna C, Cioni R, Costa A et al. (2016) MeMoVolc report on classification and dynamics of volcanic explosive eruptions. Bull Volcanol 78:84. https://doi.org/10.1007/s00445-016-1071-y

Bonadonna C, Costa A (2012) Estimating the volume of tephra deposits: A new simple strategy. Geology, 40:415–418. https://doi.org/10.1130/G32769.1

Bonadonna C, Costa A (2013) Plume height, volume, and classification of explosive volcanic eruptions based on the Weibull function. Bull Volcanol 75:742. https://doi.org/10.1007/s00445-013-0742-1

Bonadonna C, Ernst GGJ, Sparks RSJ (1998) Thickness variations and volume estimates of tephra fall deposits: the importance of particle Reynolds number. J Volcanol Geotherm Res 81:173–187. https://doi.org/10.1016/S0377-0273(98)00007-9

Bonadonna C, Houghton BF (2005) Total grain-size distribution and volume of tephra-fall deposits. Bull Volcanol 67:441–456. https://doi.org/10.1007/s00445-004-0386-2

Bonadonna C, Phillips JC (2003) Sedimentation from strong volcanic plumes. J Geophys Res 108:2340–2368

Bonadonna C, Cioni R, Pistolesi M, Connor C, Scollo S, Pioli L, Rosi M (2013) Determination of the largest clast sizes of tephra deposits for the characterization of explosive eruptions: a study of the IAVCEI Commission on Tephra Hazard Modelling. Bull Volcanol 75: 680. https://doi.org/10.1007/s00445-012-0680-3

Briffa KR, Jones PD, Schweingruber FH, Osborn TJ (1998) Influence of volcanic eruptions on Northern Hemisphere summer temperature over the past 600 years. Nature 393:450–455. https://doi.org/10.1038/30943

Burden RE, Chen L, Phillips JC (2013) A statistical method for determining the volume of volcanic fall deposits. Bull Volcanol 75:707. https://doi.org/10.1007/s00445-013-0707-4

Burden RE, Phillips JC, Hincks TK (2011) Estimating volcanic plume heights from depositional clast size, J Geophys Res 116, B11206. https://doi.org/10.1029/2011JB008548

Carey S, Sparks RSJ (1986) Quantitative models of the fallout and dispersal of tephra from volcanic eruption columns. Bull Volcanol 48:109–125. https://doi.org/10.1007/BF01046546

Cas RAF, Wright JV (1987) Volcanic Successions, Modern and Ancient. Chapman & Hall, London

Cioni R, Pistolesi M, Rosi M (2015) Plinian and Subplinian Eruptions. In Sigurdsson H, Houghton B, McNutt S, Rymer H, Stix J (eds) The Encyclopedia of Volcanoes, 2nd edn. Academic Press, London, pp 520–535

Cobeñas G, Thouret J-C, Bonadonna C, Boivin P (2012) The c.2030 yr BP Plinian eruption of El Misti volcano, Peru: Eruption dynamics and hazard implications. J Volcanol Geotherm Res 241–242:105–120. https://doi.org/10.1016/j.jvolgeores.2012.06.006

Degruyter W, Bonadonna C (2012) Improving on mass flow rate estimates of volcanic eruptions. Geophys Res Lett 39, L16308. https://doi.org/10.1029/2012GL052566

Engwell SL, Aspinall WP, Sparks RSJ (2015) An objective method for the production of isopach maps and implications for the estimation of tephra deposit volumes and their uncertainties. Bull Volcanol 77:61. https://doi.org/10.1007/s00445-015-0942-y

Fagents SA, Gregg TKP, Lopes RMC, eds. (2013) Modelling volcanic processes: the physics and mathematics of volcanism. Cambridge University Press

Fierstein J, Nathenson M (1992) Another look at the calculation of fallout tephra volumes. Bull Volcanol 54:156–167. https://doi.org/10.1007/BF00278005

Jenkins SF, Wilson T, Magill C, Miller V, Stewart C, Blong R, Marzocchi W, Boulton M, Bonadonna C, Costa A (2015) Volcanic ash fall hazard and risk. In: Loughlin SC, Sparks S, Brown SK, Jenkins SF, Vye-Brown C (eds) Global Volcanic Hazard and Risk. Cambridge University Press, pp 173–222

Juvigné E, Thouret J-C, Gilot E, Gourgaud A, Graf K, Leclercq L, Legros F, Uribe M (1997) Etude téphrostratigraphique et bio-climatique du Tardiglaciaire et de l'Holocène de la Laguna Salinas, Pérou méridional. Géogr Phys Quat 51:221–233. https://doi.org/10.7202/033120ar

Juvigné E, Thouret J-C, Loutsch I, Lamadon S, Frechen M, Fontugne M, Rivera M, Dávila J, Mariño J (2008) Retombées volcaniques dans des tourbières et lacs autour du massif des Nevados Ampato et Sabancaya (Pérou méridional, Andes Centrales). Quaternaire 19/2:157–173. https://doi.org/10.4000/quaternaire.3362

Kalnay E, Kanamitsu M, Kistler R, Collins W, Deaven D, Gandin L, Iredell M, Saha S, White G, Woollen J, Zhu Y, Leetmaa A, Reynolds R, Chelliah M, Ebisuzaki W, Higgins W, Janowiak J, Mo KC, Ropelewski C, Wang J, Jenne R, Joseph D (1996) The NCEP/NCAR 40-year reanalysis project. Bull Amer Meteor Soc 77:437–472. https://doi.org/10.1175/1520-0477(1996)077<0437:TNYRP>2.0.CO;2

Klawonn M, Houghton BF, Swanson DA, Fagents SA, Wessel P, Wolfe CJ (2014) Constraining explosive volcanism: subjective choices during estimates of eruption magnitude. Bull Volcanol 76:793. https://doi.org/10.1007/s00445-013-0793-3

Lavallée Y, de Silva SL, Salas, G, Byrnes JM (2006) Explosive volcanism (VEI 6) without caldera formation: insight from Huaynaputina volcano, southern Peru. Bull Volcanol 68:333–348. https://doi.org/10.1007/s00445-005-0010-0

Mastin LG, Guffanti M, Servranckx R, Webley P, Barsotti S, Dean K, Durant A, Ewert JW, Neri A, Rose WI, Schneider D, Siebert L, Stunder B, Swanson G, Tupper A, Volentik A, Waythomas CF (2009) A multidisciplinary effort to assign realistic source parameters to models of volcanic ash-cloud transport and dispersion during eruptions. J Volcanol Geotherm Res 186:10–21. https://doi.org/10.1016/j.jvolgeores.2009.01.008

Mix AC, Tiedemann R, Blum P (2003) Proc ODP Init Repts 202. https://doi.org/10.2973/odp.proc.ir.202.108.2003

Navarro Oviedo R (1994) Antología del valle de Omate. Universidad National San Augustín, Arequipa.

Navarro Oviedo R., Jara LA, Thouret J-C, Siebe C, Dávila J (2000) The AD 1600 eruption of Huaynaputina as described in early Spanish chronicles. Bol Soc Geol Perú 90:121–132.

Norabuena EO, Dixon TH, Stein S, Harrison CGA (1999) Decelerating Nazca-South America and Nazca-Pacific plate motions. Geophys Res Lett 26:3405–3408. https://doi.org/10.1029/1999GL005394

Oppenheimer C (2011) Eruptions that shook the World. Cambridge Univertsity Press.

Osman S, Rossi E, Bonadonna C, Frischknecht C, Andronico D, Cioni R, Scollo S (2019) Exposure-based risk assessment and emergency management associated with the fallout of large clasts at Mount Etna. Nat Hazards Earth Syst Sci https://doi.org/10.5194/nhess-2018-91

Pyle DM (1989) The thickness, volume and grainsize of tephra fall deposits. Bull Volcanol 51:1–15. https://doi.org/10.1007/BF01086757

Rivera M, Martin H, Le Pennec J-L, Thouret J-C, Gourgaud A, Gerbe MC (2017) Petro-geochemical constraints on the source and evolution of magmas at El Misti volcano (Peru). Lithos 268:240–259. https://doi.org/10.1016/j.lithos.2016.11.009

Rossi E, Bonadonna C, Degruyter W (2019) A new strategy for the estimation of plume height from clast dispersal in various atmospheric and eruptive conditions, Earth Planet Sci Lett 505:1–12, https://doi.org/10.1016/j.epsl.2018.10.007

Sandri L, Thouret JC, Constantinescu R, Biass S, Tonini R (2014) Long-term multi-hazard assessment for El Misti volcano (Peru). Bull Volcanol 76:771–796. https://doi.org/10.1007/s00445-013-0771-9

Siebert L, Simkin T, Kimberly P (2010) Volcanoes of the World, 3rd ed. University of California Press, Berkeley

Sigurdsson H, Houghton B, McNutt S, Rymer H, Stix J, eds. (2015) The Encyclopedia of Volcanoes, 2nd edn. Academic Press, London

Sparks RSJ (1986) The dimensions and dynamics of volcanic eruption columns. Bull Volcanol 48:3–15. https://doi.org/10.1007/BF01073509

Stoffel M, Khodri M, Corona C, Guillet S, Poulain V, Bekki S, Guiot J, Luckman BH, Oppenheimer C, Lebas N, Beniston M, Masson-Delmotte V (2015) Estimates of volcanic-induced cooling in the Northern Hemisphere over the past 1,500 years. Nat Geosci 8:784–788. https://doi.org/10.1038/ngeo2526

Suzuki T, Katsui Y, Nakamura T (1973) Size distribution of the Tarumai Ta-Tb pumice fall deposit. Bull Volcanol Soc Japan 18:47–63.

Thorarinsson S (1954) The eruption of Hekla, 1947-1948. Visindafelag Islendinga, Reykjavik.

Thorpe RS (1984) The tectonic setting of active Andean volcanism. In: Harmon RS, Barreiro BA (eds) Andean Magmatism. Birkhäuser Boston, pp 4–8

Thouret J-C, Davila J, Eissen J-P (1999) Largest explosive eruption in historical times in the Andes at Huaynaputina volcano, A.D. 1600, southern Peru. Geology 27:435–438. https://doi.org/10.1130/0091-7613(1999)027<0435:LEEIHT>2.3.CO;2

Thouret J-C, Finizola A, Fornari M, Suni J, Legeley-Padovani A, Frechen M (2001) Geology of El Misti volcano nearby the city of Arequipa, Peru. Geol Soc Am Bull 113:1593–1610. https://doi.org/10.1130/0016-7606(2001)113<1593:GOEMVN>2.0.CO;2

Thouret J-C, Juvigné E, Gourgaud A, Boivin P, Davila J (2002a) Reconstruction of the AD 1600 Huaynaputina eruption based on the correlation of geologic evidence with early Spanish chronicles. J Volcanol Geotherm Res 115:529–570. https://doi.org/10.1016/S0377-0273(01)00323-7

Thouret J-C, Juvigné E, Marino J, Moscol M, Loutsch I, Davila J, Legeley-Padovani A, Lamadon S, Rivera M (2002b) Late Pleistocene and Holocene tephro-stratigraphy and chronology in Southern Peru. Boletín Sociedad geológica del Perú 93:45–61.

Thouret J-C, Rivera M, Wörner G, Gerbe M-C, Finizola A, Fornari M, Gonzales K (2005) Ubinas: the evolution of the historically most active volcano in southern Peru. Bull Volcanol 67:557–589. https://doi.org/10.1007/s00445-004-0396-0

Verosub KL, Lippman J (2008) Global Impacts of the 1600 Eruption of Peru's Huaynaputina Volcano. Eos Trans AGU 89:141–142. https://doi.org/10.1029/2008EO150001

Walker GPL (1973) Explosive volcanic eruptions — a new classification scheme. Geologische Rundschau, 62:431–446. https://doi.org/10.1007/BF01840108

Walker GPL (1980) The Taupo pumice: Product of the most powerful known (ultraplinian) eruption? J Volcanol Geotherm Res 8:69–94. https://doi.org/10.1016/0377-0273(80)90008-6

Wilson L, Walker GPL (1987) Explosive volcanic eruptions - VI. Ejecta dispersal in plinian eruptions: the control of eruption conditions and atmospheric properties. Geophys J Int 89:657–679. https://doi.org/10.1111/j.1365-246X.1987.tb05186.x

Wilson M (1989) Igneous Petrogenesis: A global tectonic approach. Unwin Hyman, London

Yang Q, Bursik M (2016) A new interpolation method to model thickness, isopachs, extent, and volume of tephra fall deposits. Bull Volcanol 78:68. https://doi.org/10.1007/s00445-016-1061-0

Figures

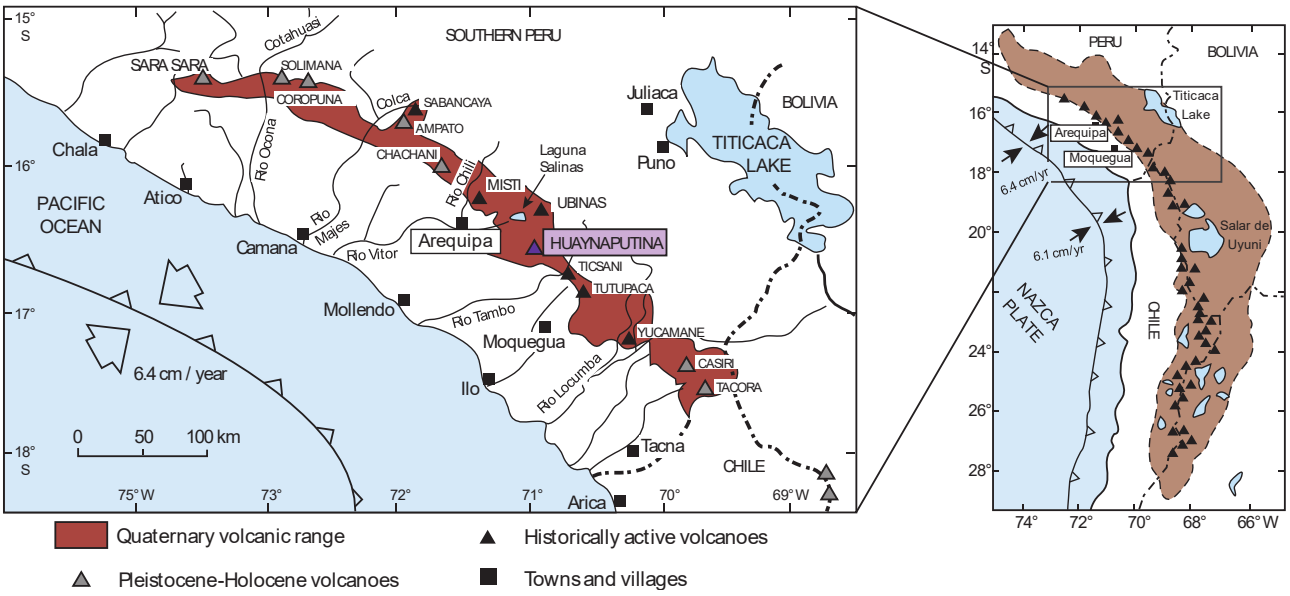

Figure 1 Geological setting of the present volcanic range in southern Peru with emphasis on historically active volcanoes. Inset: The Central Andean Volcanic Zone. From Thouret et al. (2005)

Figure 2 Regional impacts of the CE 1600 Huaynaputina eruption. From Navarro Oviedo et al. (2000)

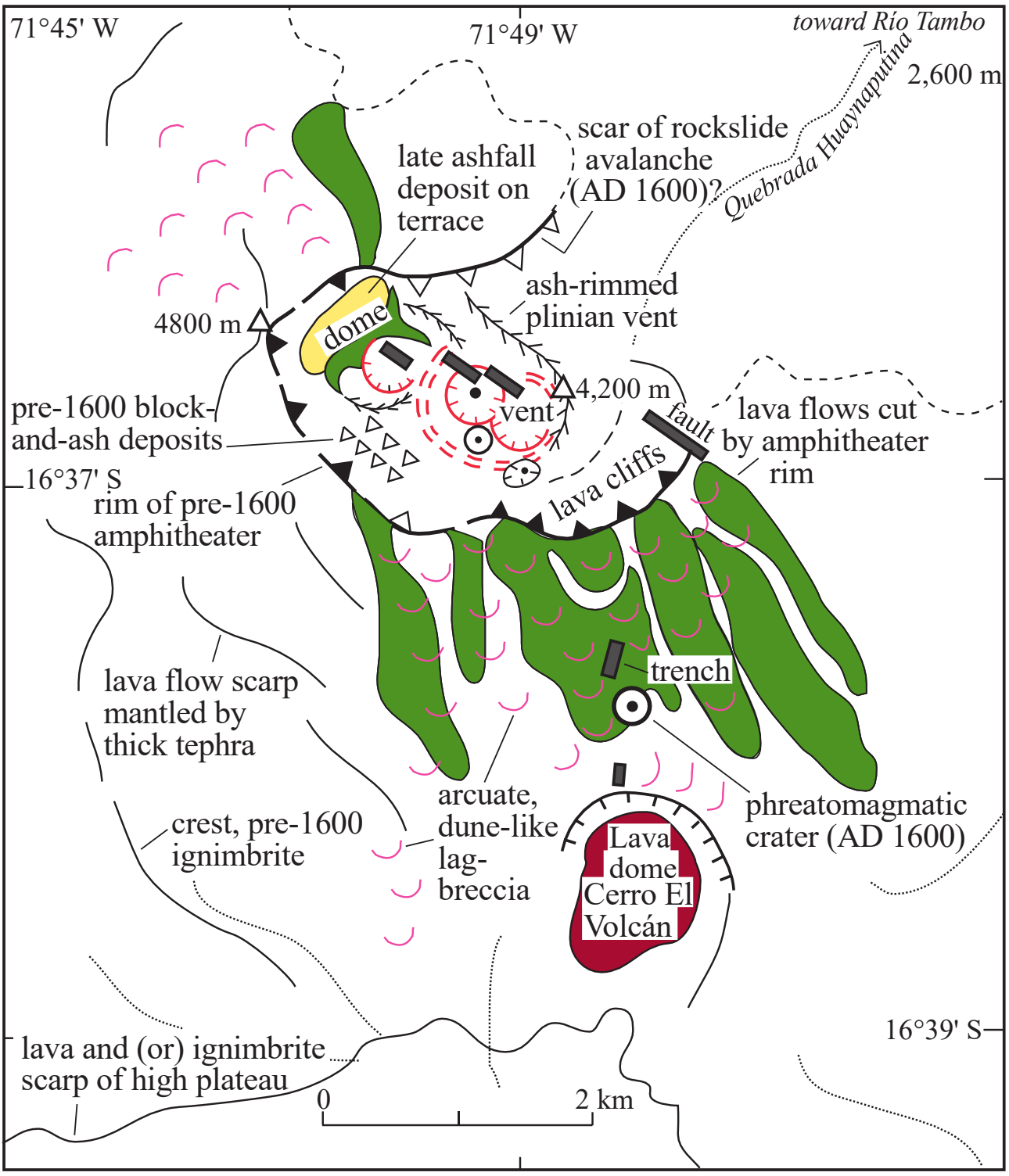

Figure 3 Sketch map (based on a satellite SPOT image) showing the crater complex nested in a horseshoe-shaped amphitheatre, and pre-1600 features. Ring fractures cut through the amphitheatre floor as well as three craters. From Thouret et al. (2002a)

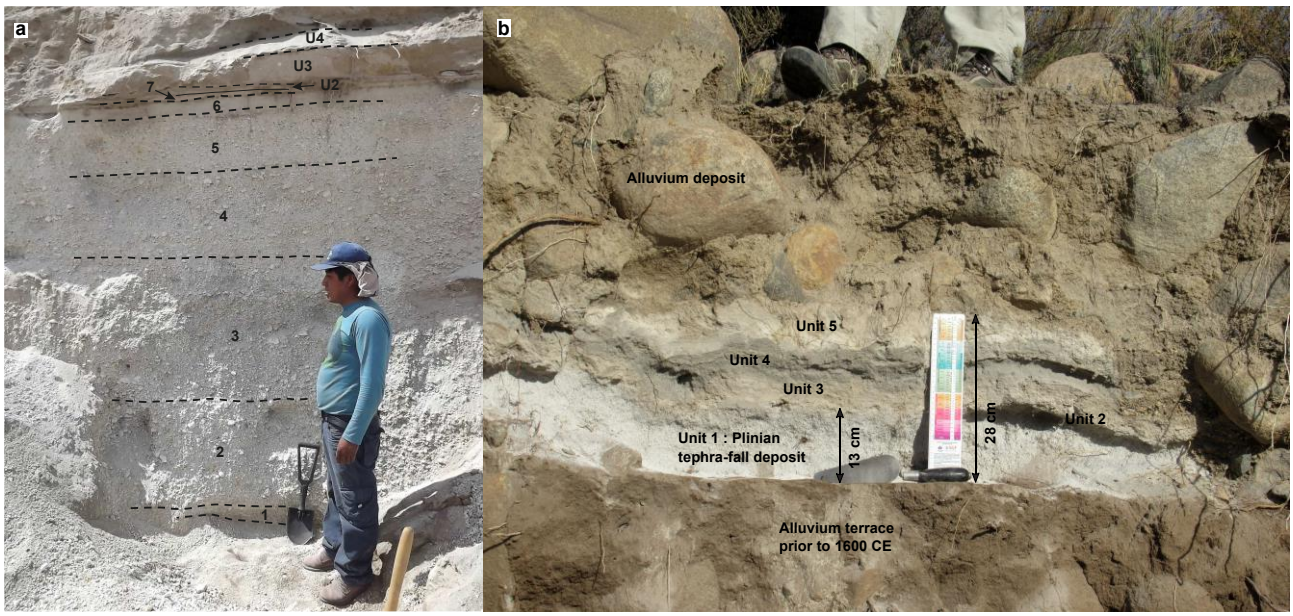

Figure 4 (a) Proximal facies of Unit 1 at the Quinistacas Football Club stadium, 12.5 km WSW from the vent. The deposit is 280 cm thick and includes seven subunits. (b) Distal tephra section in Yarabamba, 65 km west from the vent. Five distinct tephra units are shown, including the Plinian tephra-fall layer at the base

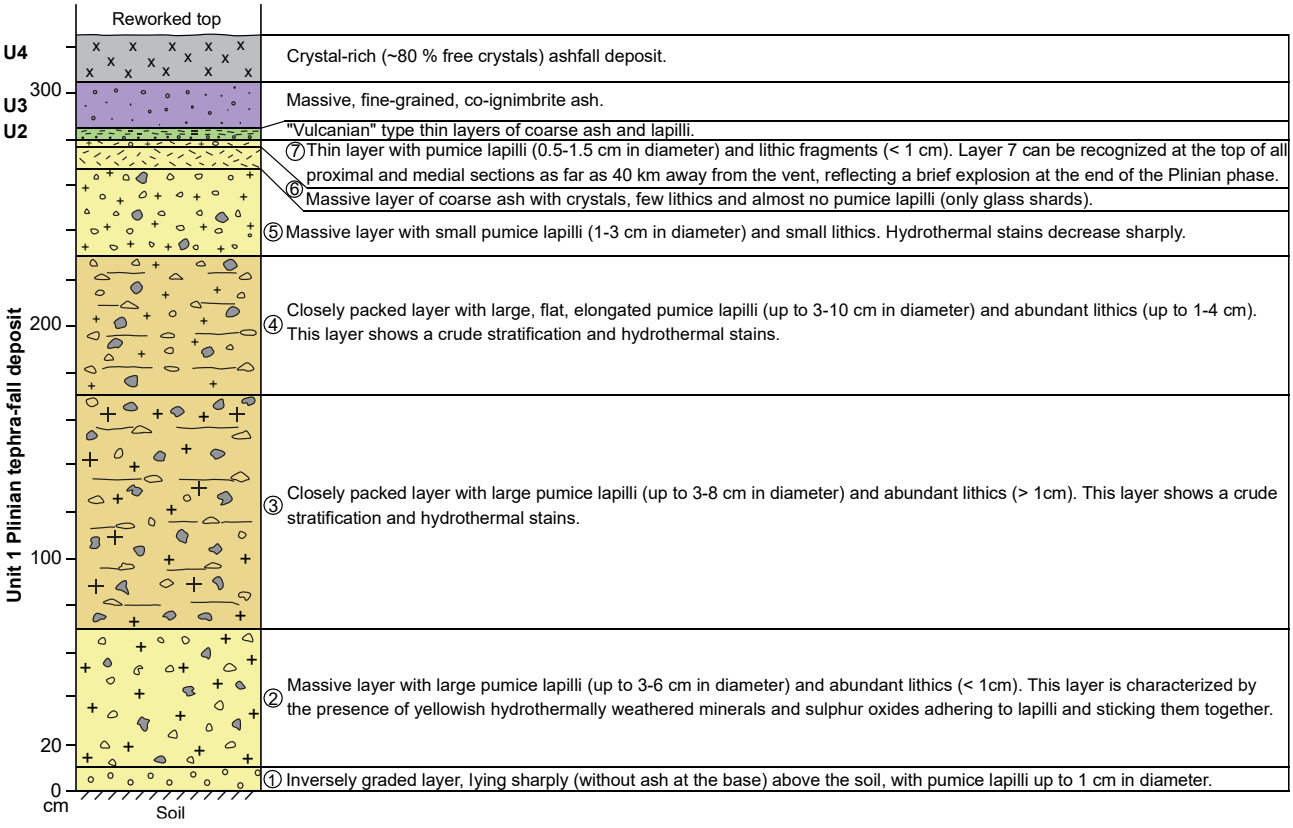

Figure 5 Section of the Plinian tephra-fall deposit at the Quinistacas Football Club stadium, 12.5 km WSW from the vent, with description of the seven subunits

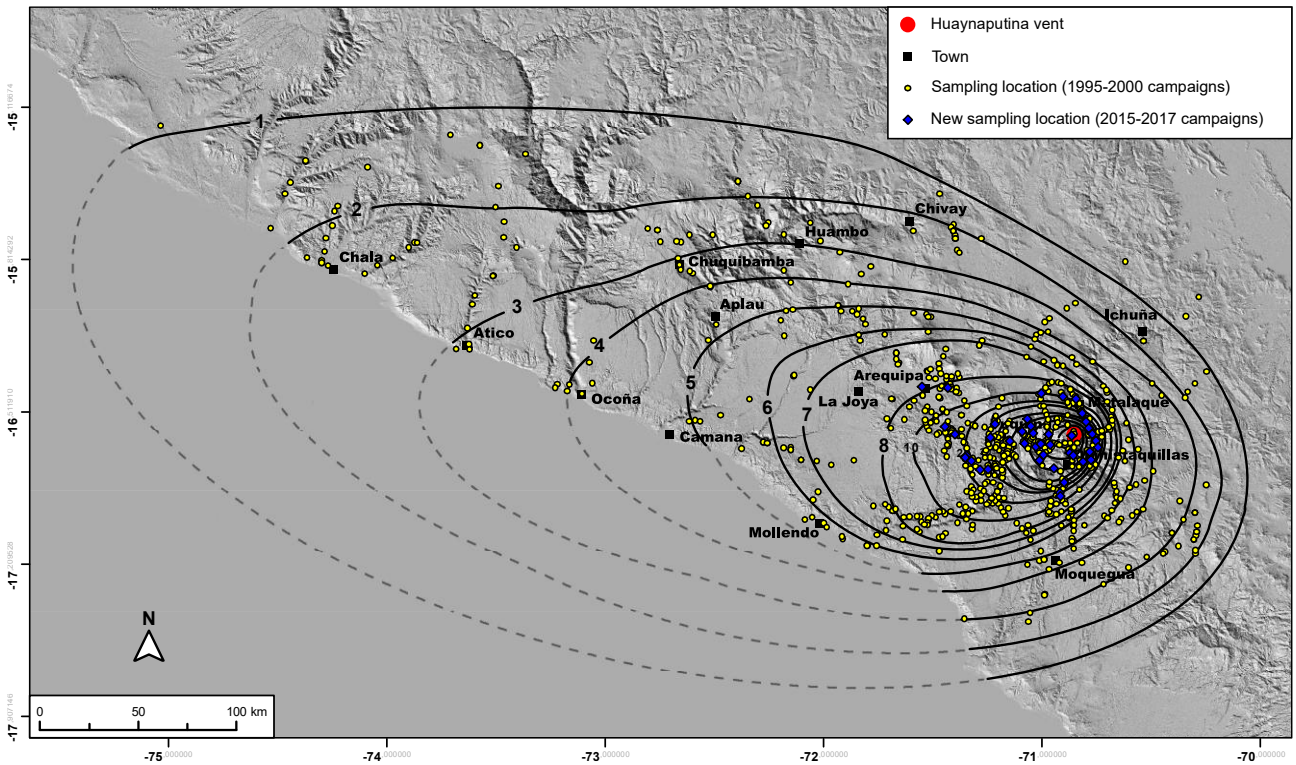

Figure 6 Revised isopach map of the Huaynaputina 1600 CE tephra-fall deposit (Unit 1) including new field data collected in 2015–2017, draped over the ASTER Global Digital Elevation Model version 2 (a product of NASA and METI). Thickness is in cm, coordinates are in decimal degrees

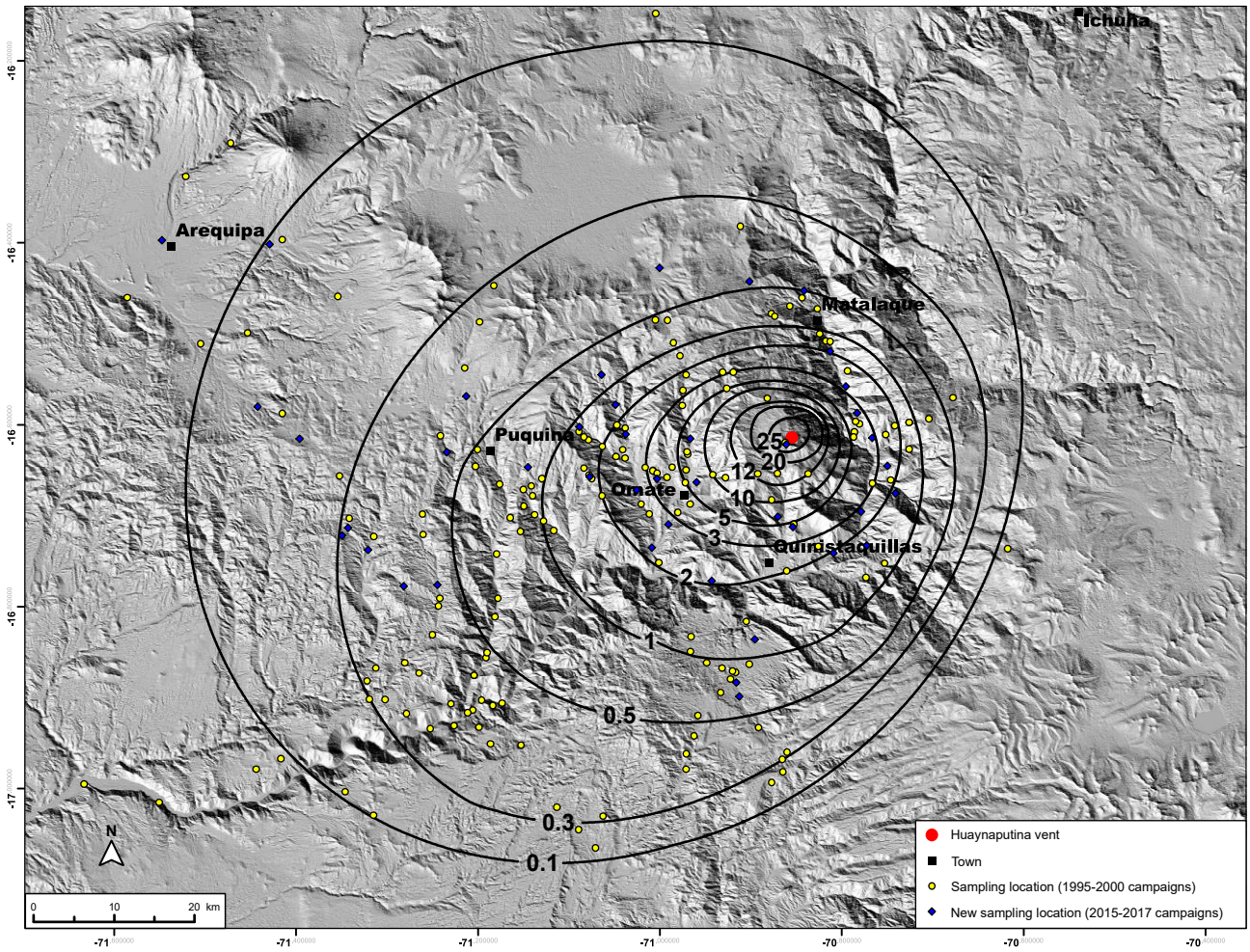

Figure 7 Unit 1 maximum lithics isopleth map revised with 2015–2017 data, draped over the ASTER Global

Digital Elevation Model version 2 (a product of NASA and METI). Grain-size is in cm, coordinates are in decimal degrees

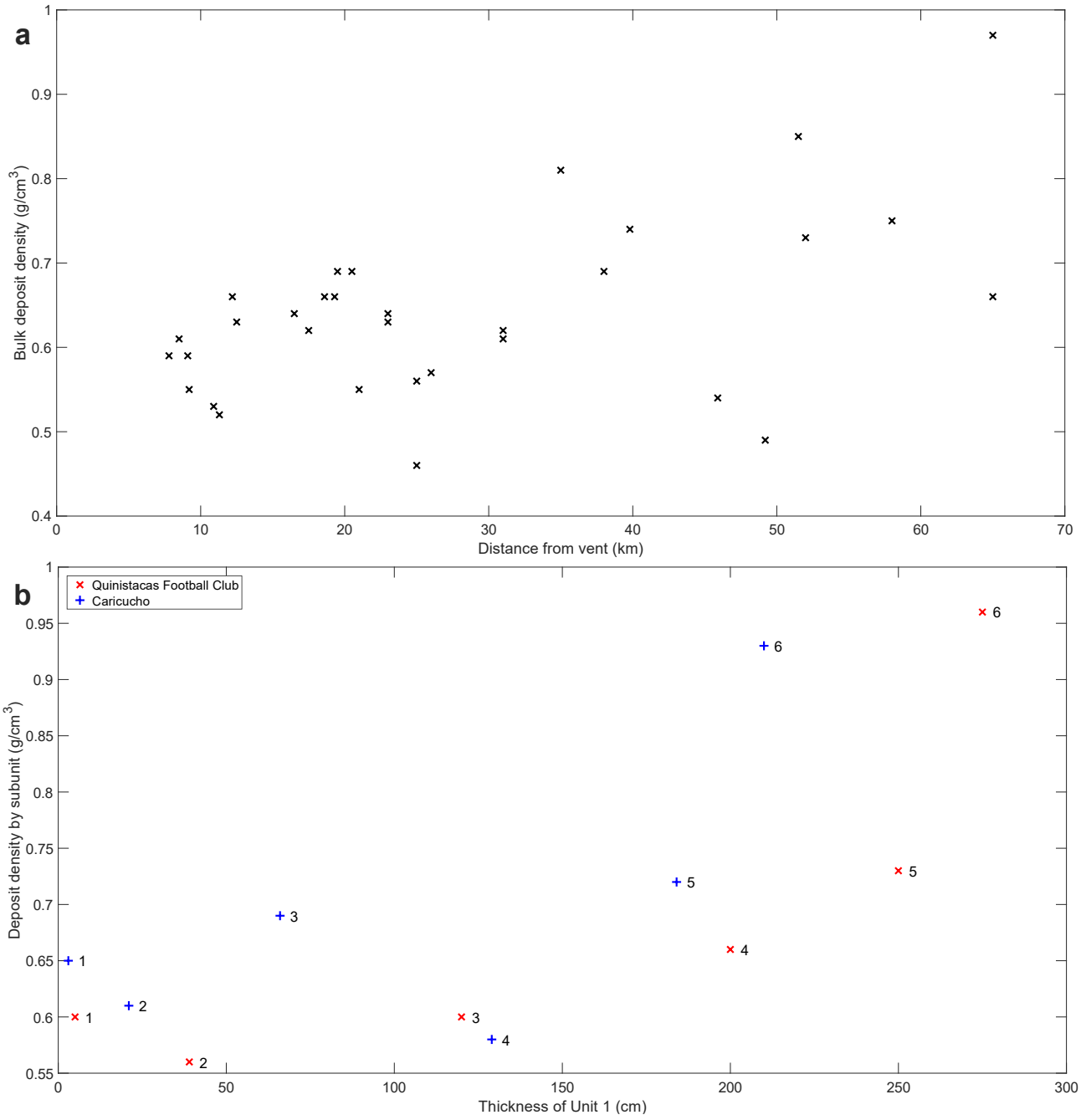

Figure 8 (a) Variation of Unit 1 bulk deposit density with distance from the vent. (b) Variation of deposit density across the six subunits at QFC (red) and Caricucho (blue)

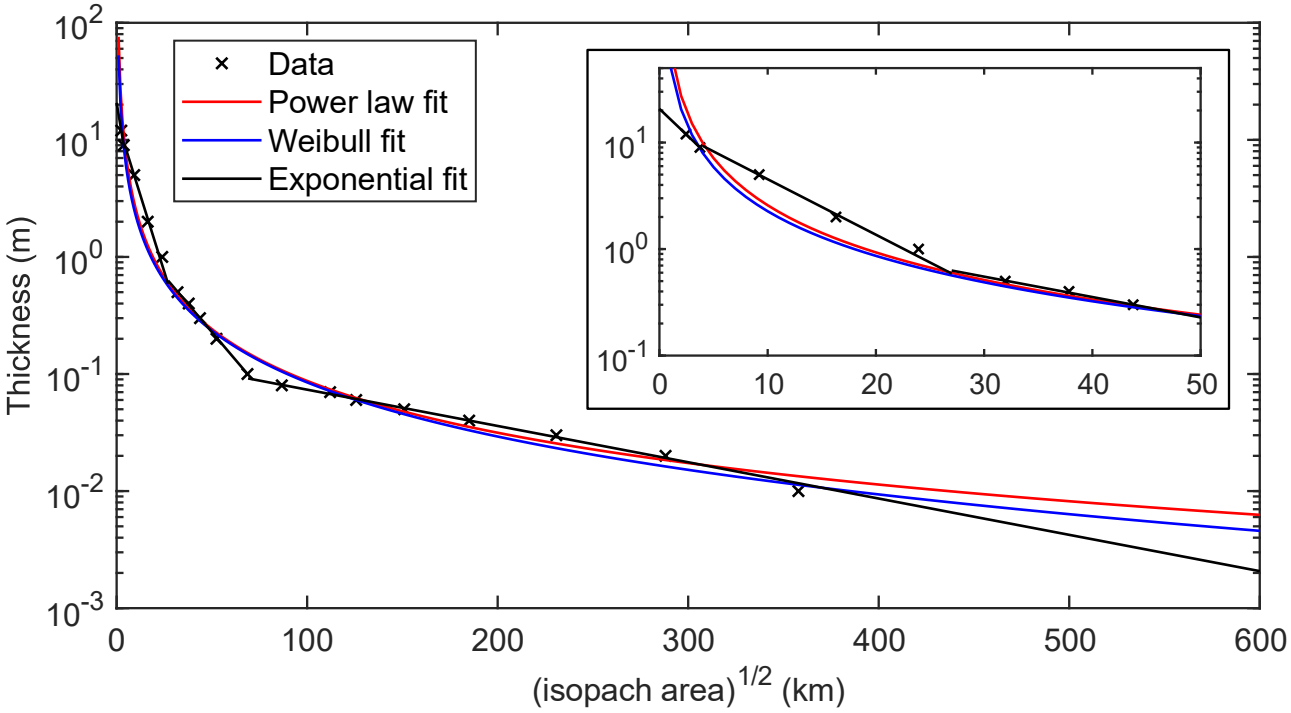

Figure 9 Semi-log plot of thickness vs. square root of isopach area with exponential (four segments), power law and Weibull best fits. Inset: enlarged version focusing on the near-vent area

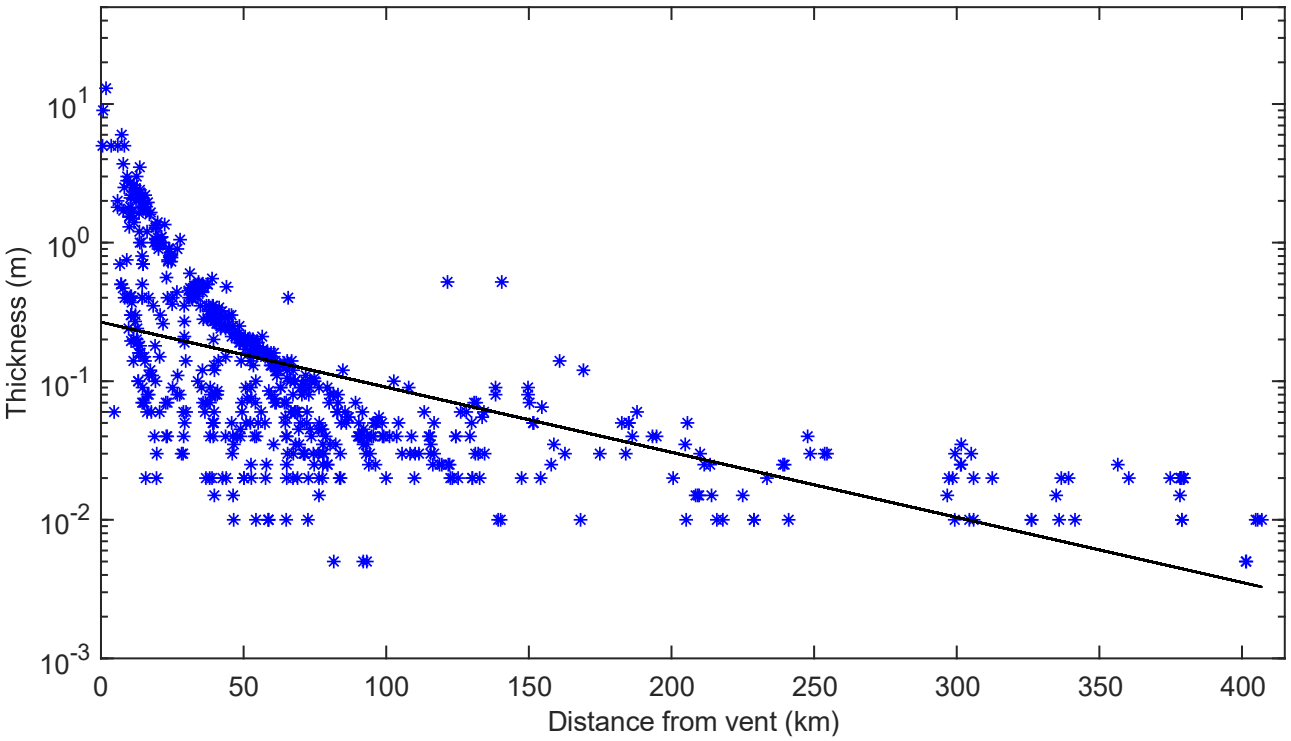

Figure 10 Scatter plot of thickness data (blue, in log scale) versus distance from vent, and corresponding linear regression (black)

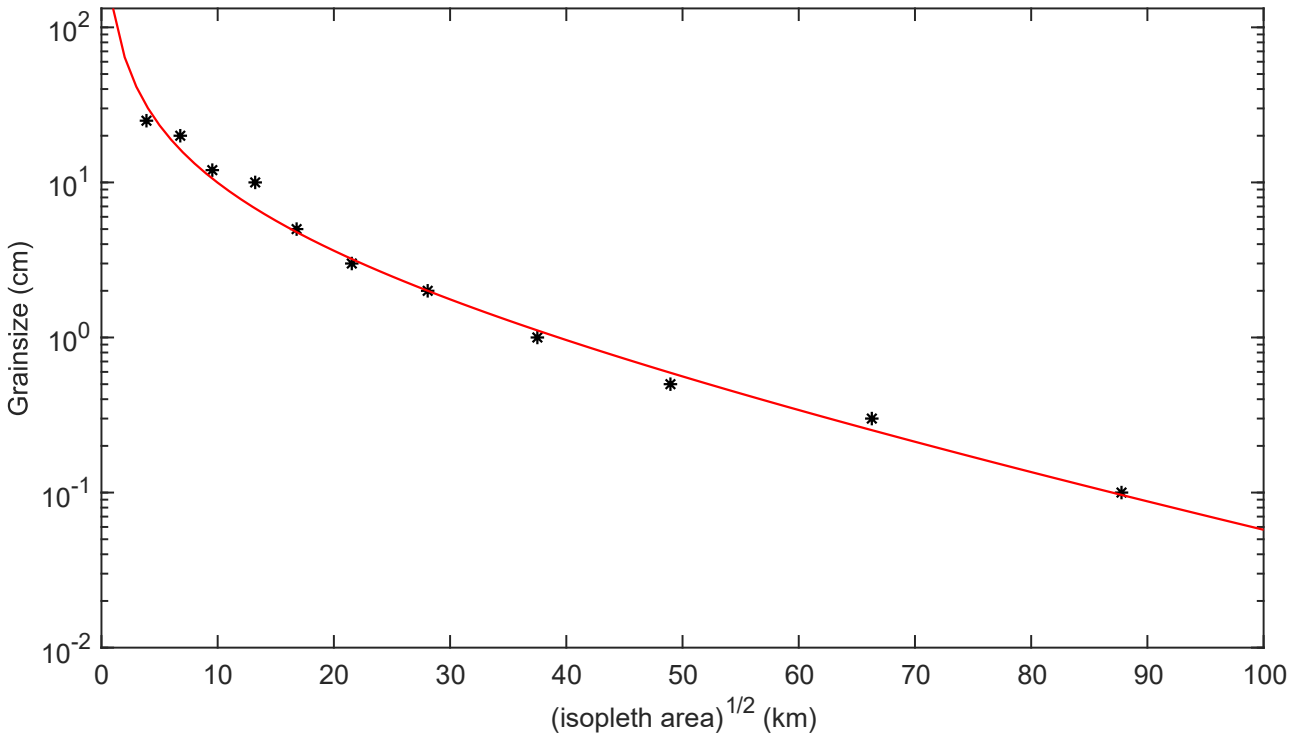

Figure 11 Semi-log plot of grain size vs. square root of isopleth area, and corresponding Weibull fit

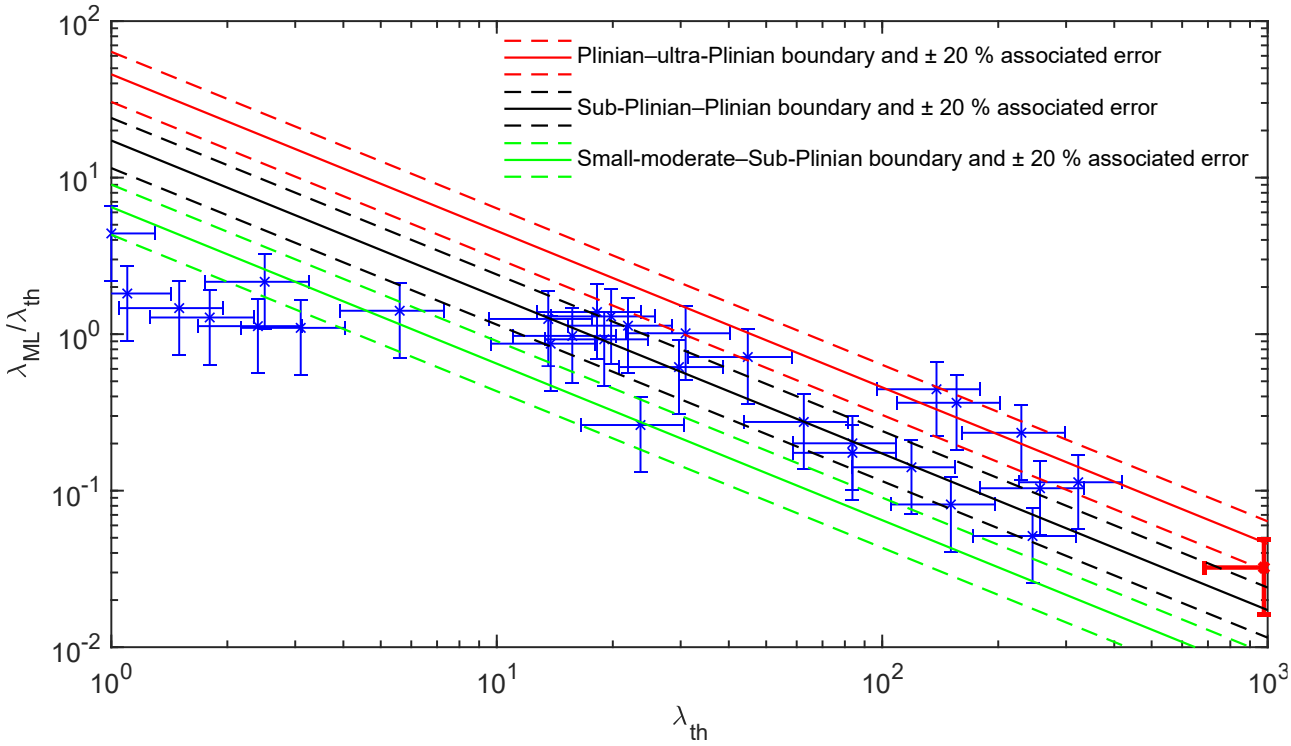

Figure 12 Unit 1 Weibull parameters λ_{th} and λ_{ML} (red) plotted on Bonadonna and Costa (2013) classification scheme with 30 eruptions from the literature (blue). Error bars are ± 30 % for the estimation of λ_{th} and ± 50 % for $\lambda_{ML}/\lambda_{th}$

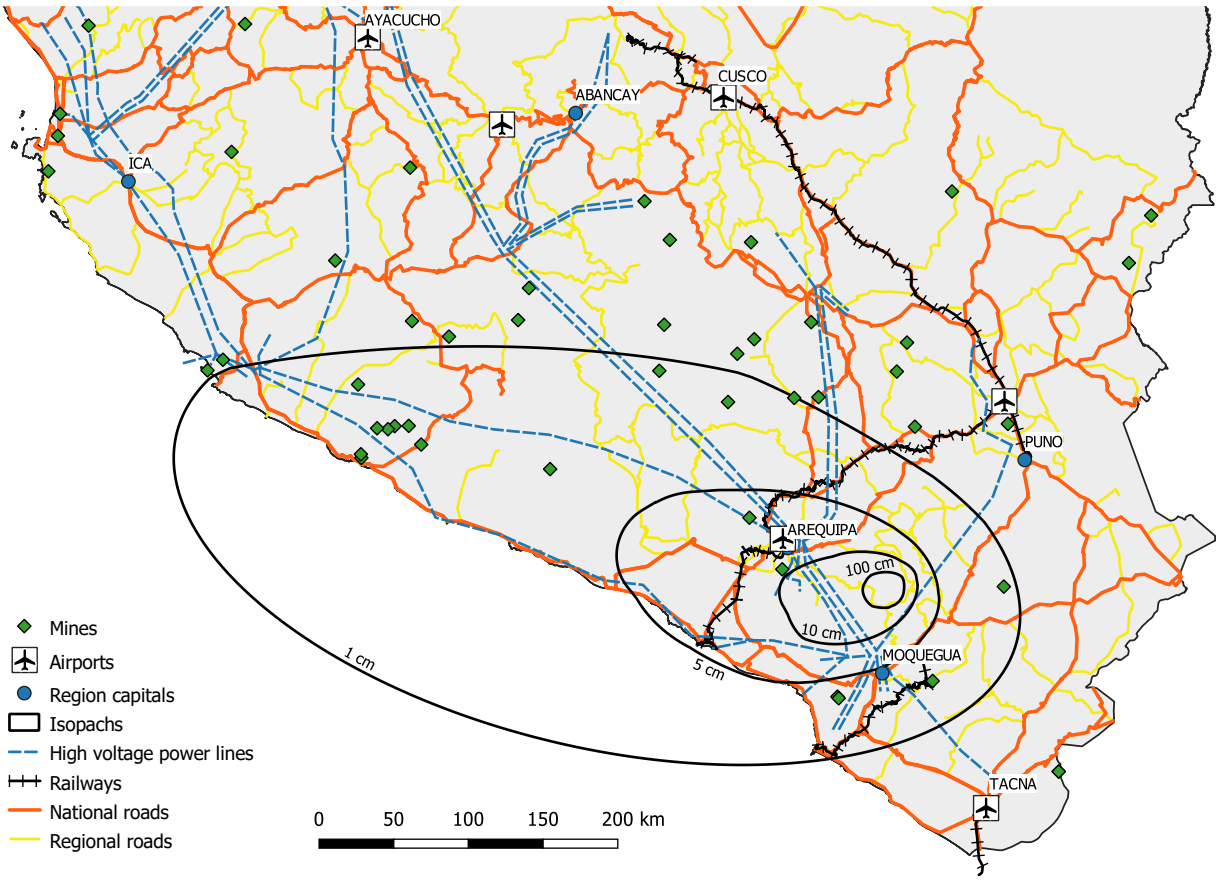

Figure 13 Map of current infrastructures in South Peru, along with selected isopachs of Huaynaputina 1600 CE eruption. Sources: Ministerio de Transportes y Comunicaciones, Ministerio de Energía y Minas, Comité de Operación Económica del Sistema

Tables

Method	Volume (km^3)	Parameter (unit)	Value
Exponential	8.2		
Segment 1	0.8	k_1	0.223000
		$T1_0$ (m)	20.7200
		BS_1 (km)	4
Segment 2	1.1	k_2	0.12
		$T2_0$ (m)	15.0300
		BS_2 (km)	28
Segment 3	0.9	k_3	0.044080
		$T3_0$ (m)	2.0670
		BS_3 (km)	69
Segment 4	5.4	k_4	0.007138
		$T4_0$ (m)	0.1501
Power law	13.3 (10.6–15.6)		
		T_{pl}	76.02
		m	1.47
		B (km)	3
		C (km)	1500 (1000–2000)
Weibull	14.4		
		θ_{th} (cm)	0.49
		λ_{th} (km)	978
		n_{th}	0.65
Bayesian linear regression	14.3		
		A	-8.228821
		B	-0.01081147
		σ^2	$7.476968\ 10^{-6}$

Table 1 Fit parameters of the exponential, power law, Weibull and Bayesian linear regression methods, and associated volume estimates. For the power-law method, we have used a range of values for *C* to assess the uncertainty on volume estimate (Bonadonna and Houghton 2005). It is important to note that 2091 km from the vent (square root of area) corresponds to a deposit thickness of 1 mm

Isopleth (cm)	Downwind range (km)	Crosswind range (km)	Plume height C&S86 (km)	Wind speed (m s^{-1})	Plume height R19 (km)
1	30	19	35.5	17	28.4
2	23	13	32.4	21	26.2
3	18	11	31.8	19	28.2
5	14	9	32.2	17	30.6
		Mean	33.0	18.5	28.4

Table 2 Plume height and wind speed estimates using Biass et al. (2015) MatLab implementation of Carey and Sparks (1986) method and Rossi et al. (2019) model